

Impact of model parameters on Monte Carlo simulations of backscattering Mueller matrix images of colon tissue

Maria-Rosaria Antonelli,^{1,*} Angelo Pierangelo,¹ Tatiana Novikova,¹ Pierre Validire,² Abdelali Benali,² Brice Gayet,³ and Antonello De Martino¹

¹LPICM, Ecole polytechnique, CNRS, 91128 Palaiseau, France

²Département d'Anatomopathologie de l'Institut Mutualiste Montsouris, 42 Bd Jourdan, 75014 Paris, France

³Département médico-chirurgical de pathologie digestive de l'Institut Mutualiste Montsouris 42 Bd Jourdan, 75014 Paris, France

*antonellirosaria@hotmail.it

Abstract: Polarimetric imaging is emerging as a viable technique for tumor detection and staging. As a preliminary step towards a thorough understanding of the observed contrasts, we present a set of numerical Monte Carlo simulations of the polarimetric response of multilayer structures representing colon samples in the backscattering geometry. In a first instance, a typical colon sample was modeled as one or two scattering “slabs” with monodisperse non absorbing scatterers representing the most superficial tissue layers (the mucosa and submucosa), above a totally depolarizing Lambertian lumping the contributions of the deeper layers (muscularis and pericolic tissue). The model parameters were the number of layers, their thicknesses and morphology, the sizes and concentrations of the scatterers, the optical index contrast between the scatterers and the surrounding medium, and the Lambertian albedo. With quite similar results for single and double layer structures, this model does not reproduce the experimentally observed stability of the relative magnitudes of the depolarizing powers for incident linear and circular polarizations. This issue was solved by considering bimodal populations including large and small scatterers in a single layer above the Lambertian, a result which shows the importance of taking into account the various types of scatterers (nuclei, collagen fibers and organelles) in the same model.

©2011 Optical Society of America

OCIS codes: (110.5405) Polarimetric imaging; (170.3880) Medical and biological imaging; (260.5430) Polarization; (290.4210) Multiple scattering; (290.4020) Mie theory; (000.4430) Numerical approximation and analysis.

References and links

1. I. A. Vitkin, R. D. Laszlo, and C. L. Whyman, “Effects of molecular asymmetry of optically active molecules on the polarization properties of multiply scattered light,” *Opt. Express* **10**(4), 222–229 (2002).
2. X. Guo, M. F. G. Wood, and I. A. Vitkin, “Angular measurements of light scattered by turbid chiral media using linear Stokes polarimeter,” *J. Biomed. Opt.* **11**(4), 041105 (2006).
3. M. F. G. Wood, X. Guo, and I. A. Vitkin, “Polarized light propagation in multiply scattering media exhibiting both linear birefringence and optical activity: Monte Carlo model and experimental methodology,” *J. Biomed. Opt.* **12**(1), 014029 (2007).
4. N. Ghosh, M. F. G. Wood, and I. A. Vitkin, “Mueller matrix decomposition for extraction of individual polarization parameters from complex turbid media exhibiting multiple scattering, optical activity, and linear birefringence,” *J. Biomed. Opt.* **13**(4), 044036 (2008).
5. N. Ghosh, M. F. G. Wood, and I. A. Vitkin, “Polarimetry in turbid, birefringent, optically active media: a Monte Carlo study of Mueller matrix decomposition in the backscattering geometry,” *J. Appl. Phys.* **105**(10), 102023 (2009).
6. M. F. G. Wood, N. Ghosh, E. H. Moriyama, B. C. Wilson, and I. A. Vitkin, “Proof-of-principle demonstration of a Mueller matrix decomposition method for polarized light tissue characterization in vivo,” *J. Biomed. Opt.* **14**(1), 014029 (2009).

7. V. V. Tuchin, L. Wang, and D. A. Zimnyakov, *Optical Polarization in Biomedical Applications* (Springer-Verlag, Berlin, 2006).
8. V. V. Tuchin, *Tissue Optics: Light Scattering Methods and Instruments for Medical Diagnosis*, 2nd ed., SPIE Press Monograph Vol. PM166 (SPIE, Bellingham, WA, 2007).
9. H. H. Tynes, G. W. Kattawar, E. P. Zege, I. L. Katsev, A. S. Prikhach, and L. I. Chaikovskaya, "Monte Carlo and multicomponent approximation methods for vector radiative transfer by use of effective Mueller matrix calculations," *Appl. Opt.* **40**(3), 400–412 (2001).
10. I. L. Maksimova, S. V. Romanov, and V. F. Izotova, "The effect of multiple scattering in disperse media on polarization characteristics of scattered light," *Opt. Spectrosc.* **92**(6), 915–923 (2002).
11. S. L. Jacques, R. Samatham, S. Isenath, and K. Lee, "Polarized light camera to guide surgical excision of skin cancers," *Proc. SPIE* **6842**, 68420I, 68420I-7 (2008).
12. M. Anastasiadou, S. Ben Hatit, R. Ossikovski, S. Guyot, and A. De Martino, "Experimental validation of the reverse polar decomposition of depolarizing Mueller matrices," *J. European Opt. Soc. Rapid Publications* **2**, 07018 (2007).
13. A. H. Hielscher, J. R. Mourant, and I. J. Bigio, "Influence of particle size and concentration on the diffuse backscattering of polarized light from tissue phantoms and biological cell suspensions," *Appl. Opt.* **36**(1), 125–135 (1997).
14. M. R. Antonelli, A. Pierangelo, T. Novikova, P. Validire, A. Benali, B. Gayet, and A. De Martino, "Mueller matrix imaging of human colon tissue for cancer diagnostics: how Monte Carlo modeling can help in the interpretation of experimental data," *Opt. Express* **18**(10), 10200–10208 (2010).
15. A. H. Hielscher, A. A. Eick, J. R. Mourant, D. Shen, J. P. Freyer, and I. J. Bigio, "Diffuse backscattering Mueller matrices of highly scattering media," *Opt. Express* **1**(13), 441–453 (1997).
16. M. H. Smith, P. Burke, A. Lompad, E. Tanner, and L. W. Hillman, "Mueller matrix imaging polarimetry in dermatology," *Proc. SPIE* **3911**, 210–216 (2000).
17. M. Smith, "Interpreting Mueller matrix images of tissues," *Proc. SPIE* **4257**, 82–89 (2001).
18. J. C. Ramella-Roman, S. A. Prahl, and S. L. Jacques, "Three Monte Carlo programs of polarized light transport into scattering media: part I," *Opt. Express* **13**(12), 4420–4438 (2005).
19. A. Pierangelo, A. Benali, M. R. Antonelli, T. Novikova, P. Validire, B. Gayet, and A. De Martino, "Ex-vivo characterization of human colon cancer by Mueller polarimetric imaging," *Opt. Express* **19**(2), 1582–1593 (2011).
20. A. Pierangelo, S. Manhas, A. Benali, M. R. Antonelli, T. Novikova, P. Validire, B. Gayet, A. De Martino, and P. Validire, "Use of Mueller imaging for the staging of human colon cancer," *Proc. SPIE* **7895**, 78950E (2011).
21. V. Sankaran, J. T. Walsh, Jr., and D. J. Maitland, "Comparative study of polarized light propagation in biologic tissues," *J. Biomed. Opt.* **7**(3), 300–306 (2002).
22. A. Pierangelo, A. De Martino, M. Anastasiadou, P. Validire, B. Huynh, H. Cohen, and L. Schwartz, "Multispectral Mueller imaging of ex-vivo tissue," in *Proceedings of the European 1st NanoCharM Workshop on Polarization-Based Optical Techniques Applied to Biology and Medicine* (nanocharm.org, 2009), pp. 32–38, <http://www.nanocharm.org/images/stories/Library/Proceedings/1st%20Workshop/1stWorkshopProceedings.pdf>.
23. L. T. Perelman, V. Backman, M. Wallace, G. Zonios, R. Manoharan, A. Nusrat, S. Shields, M. Seiler, C. Lima, T. Hamano, I. Itzkan, J. Van Dam, J. M. Crawford, and M. S. Feld, "Observation of periodic fine structure in reflectance from biological tissue: a new technique for measuring nuclear size distribution," *Phys. Rev. Lett.* **80**(3), 627–630 (1998).
24. G. Zonios, L. T. Perelman, V. Backman, R. Manoharan, M. Fitzmaurice, J. Van Dam, and M. S. Feld, "Diffuse reflectance spectroscopy of human adenomatous colon polyps in vivo," *Appl. Opt.* **38**(31), 6628–6637 (1999).
25. K. Badizadegan, V. Backman, C. W. Boone, C. P. Crum, R. R. Dasari, I. Georgakoudi, K. Keefe, K. Munger, S. M. Shapshay, E. E. Sheets, and M. S. Feld, "Spectroscopic diagnosis and imaging of invisible pre-cancer," *Faraday Discuss.* **126**, 265–279, discussion 303–311 (2004).
26. D. Hidović-Rowe and E. Claridge, "Modelling and validation of spectral reflectance for the colon," *Phys. Med. Biol.* **50**(6), 1071–1093 (2005).
27. B. Kaplan, G. Ledanois, and B. Dréysson, "Mueller matrix of dense polystyrene latex sphere suspensions: measurements and Monte Carlo simulation," *Appl. Opt.* **40**(16), 2769–2777 (2001).
28. J.-M. André, M. Catala, J.-J. Morère, E. Escudier, G. Katsanis, and J. Poirier, "Histologie: les tissus," (Faculté de Médecine, Université Pierre et Marie Curie, PAES) (2007–2008), <http://www.chups.jussieu.fr/polys/histo/histoP1/histoP1.pdf/>.
29. S. A. Skinner and P. E. O'Brien, "The microvascular structure of the normal colon in rats and humans," *J. Surg. Res.* **61**(2), 482–490 (1996).
30. H. C. van de Hulst, *Light Scattering by Small Particles* (Dover, New York, 1981).
31. G. I. Zonios, R. M. Cothren, J. T. Arendt, J. Wu, J. Van Dam, J. M. Crawford, R. Manoharan, and M. S. Feld, "Morphological model of human colon tissue fluorescence," *IEEE Trans. Biomed. Eng.* **43**(2), 113–122 (1996).
32. M. Lualdi, A. Colombo, B. Farina, S. Tomatis, and R. Marchesini, "A phantom with tissue-like optical properties in the visible and near infrared for use in photomedicine," *Lasers Surg. Med.* **28**(3), 237–243 (2001).
33. J. C. Ramella-Roman, S. A. Prahl, and S. L. Jacques, "Three Monte Carlo programs of polarized light transport into scattering media: part I," *Opt. Express* **13**(12), 4420–4438 (2005).
34. J. C. Ramella-Roman, S. A. Prahl, and S. L. Jacques, "Three Monte Carlo programs of polarized light transport into scattering media: part II," *Opt. Express* **13**(25), 10392–10405 (2005).
35. R. Graaff, M. H. Koelink, F. F. M. de Mul, W. G. Zijlstra, A. C. M. Dassel, and J. G. Aarnoudse, "Condensed Monte Carlo simulations for the description of light transport," *Appl. Opt.* **32**(4), 426–434 (1993).

36. A. Kienle and M. S. Patterson, "Determination of the optical properties of turbid media from a single Monte Carlo simulation," *Phys. Med. Biol.* **41**(10), 2221–2227 (1996).
37. A. Sassaroli, C. Blumetti, F. Martelli, L. Alianelli, D. Contini, A. Ismaelli, and G. Zaccanti, "Monte carlo procedure for investigating light propagation and imaging of highly scattering media," *Appl. Opt.* **37**(31), 7392–7400 (1998).
38. A. N. Bashkatov, E. A. Genina, V. I. Kochubey, and V. V. Tuchin, "Estimation of wavelength dependence of refractive index of collagen fibers of scleral tissue," *Proc. SPIE* **4162**, 265–268 (2000).
39. A. N. Bashkatov and E. A. Genina, "Water refractive index in dependence on temperature and wavelength: a simple approximation," *Proc. SPIE* **5068**, 393–395 (2003).
40. "Research in Biomedical Optics," MIT spectroscopy, <http://web.mit.edu/spectroscopy/research/biomedicaloptics.html>.
41. H. J. van Staveren, C. J. M. Moes, J. van Marie, S. A. Prahl, and M. J. C. van Gemert, "Light scattering in Intralipid-10% in the wavelength range of 400-1100 nm," *Appl. Opt.* **30**(31), 4507–4514 (1991).
42. R. L. P. van Veen, W. Verkruyse, and H. J. C. M. Sterenborg, "Diffuse-reflectance spectroscopy from 500 to 1060 nm by correction for inhomogeneously distributed absorbers," *Opt. Lett.* **27**(4), 246–248 (2002).
43. L. O. Svaasand, E. J. Fiskerstrand, G. Kopstad, L. T. Norvang, E. K. Svaasand, J. S. Nelson, and M. W. Berns, "Therapeutic response during pulsed laser treatment of port-wine stains: dependence on vessel diameter and depth in dermis," *Lasers Med. Sci.* **10**(4), 235–243 (1995).
44. S. Prahl, "Optical Absorption of Hemoglobin" (Oregon Medical Laser Center, Portland, OR) (1999) <http://omlc.ogi.edu/spectra/hemoglobin/>.
45. H. Du, R.-C. A. Fuh, J. Li, L. A. Corkan, and J. S. Lindsey, "PhotochemCAD: a computer-aided design and research tool in photochemistry," *Photochem. Photobiol.* **68**(2), 141–142 (1998).

1. Introduction

The interaction of light with matter may be characterized in a number of ways, such as transmission, absorption, reflection, spontaneous emission and scattering. Polarimetric imaging is based on the analysis of the modification of the incident light *polarization* due to interaction with the sample. As such, it may provide different and complementary information with respect to the usual imaging based on *intensity* measurements. Among many other topics, the detection and measurement of weak optical activity in samples of biomedical interest is being actively investigated [1–6], in connection with the development of fast and non-invasive techniques to measure blood sugar levels.

However, the interpretation of polarimetric data may require specific modeling, especially for samples such as biological tissues, where the light typically suffers multiple scatterings before being eventually detected. This general topic of tissue measurements with polarized light and the related modeling is reviewed in Refs. [7,8].

On the theoretical side, for multiscattering media one has to solve the Vector Radiative Transfer Equation (VRTE), which is established from local detailed energetic balance, and which may be solved in a number of ways [9,10], including Monte Carlo algorithms such as the one used in this work.

From the experimental point of view, polarimetric imaging may be implemented in several ways, based on various ways to generate the incident polarization and to analyze its counterpart of the emerging light. For example, only two images are required for Orthogonal State Contrast (OSC). These two images are typically taken with parallel and perpendicular linear polarizations, and then combined to display the (somewhat improperly called) Degree Of Linear Polarization (DOLP). The same approach may be applied to orthogonal states of circular polarization, to display the Degree of Circular Polarization, or DOCP. These techniques provide contrasts which may be useful in various fields, e.g. in dermatology [11]. However, OSC techniques can completely characterize only special samples, with simple polarimetric responses, such as pure depolarizers. Conversely, in the most general case, a complete characterization of the sample requires Mueller polarimetry, which is based on the acquisition of 16 images (with four input and four output polarization states). These images can subsequently be treated by various algorithms to "extract" the essential polarimetric effects, namely the diattenuation, the retardation and the depolarization [6,12].

Mueller images of turbid media taken in the backscattering geometry with a point source illumination revealed that this technique is sensitive to the size of polystyrene spheres in water [13,14]. Hielscher *et al.* demonstrated that the Mueller matrix imaging can differentiate between normal and tumoral cell suspensions [15]. These results, together with other

investigations [16,17] provide evidence of the potential of Mueller matrix imaging in backscattering geometry for medical applications and more particularly for cancer detection and staging [18–20].

On the other hand the tissue features responsible for the observed contrasts between healthy and cancerous tissues are by no means obvious. The development of cancer is associated with an increase of the size of cell nuclei, a disruption of the tissue structure, and an increase of its thickness and blood content. These effects are respectively due to accelerated cell proliferation, reduced apoptosis and neovascularization.

However, when cancer starts to develop, many different processes get activated inside the cells as well as in the interstitial tissue. These processes may modify the biochemical content of the intracellular and extracellular environment and thus change the optical properties of the tissue. In this regard, we investigated in a previous work [14] how the index contrast between monodisperse scatterers and the surrounding medium affects the regime of scattering. The essential result was the onset of the Rayleigh-Gans scattering regime for the small index contrasts typical of nuclei versus cytoplasm. In this regime large (compared to wavelength) spheres behave as small objects (Rayleigh regime), in agreement with experimental studies of many tissues [20–22]. This also implies that the common studies on tissue phantoms with large contrast of index between the scatterers and the surrounding medium may not be relevant for realistic simulations of the polarimetric response of typical biological tissues.

A thorough understanding of light propagation in scattering media is thus essential to model polarized light scattering in tissues with the required accuracy for diagnostic purposes. Both theoretical [23–25] and numerical [26] approaches have been used to describe light scattering in colon samples. In particular D. Hidović-Rowe and E. Claridge [26] proposed a detailed model of colon tissue, where collagen is the main scatterer. They used the Monte Carlo method to simulate diffuse spectral reflectance of colon tissue.

In this study initially we used the model of colon tissue proposed in [26] to describe healthy colon samples. We performed Monte Carlo calculations, using the method illustrated in details elsewhere [14,27], to simulate the propagation of polarized light in multi-scattering media. We present the results of the simulations for the scattering in backward geometry and we investigate the impact of all model parameters on the optical response of the colon sample. Based on above mentioned investigations and comparisons with experimental data the necessary model modifications were proposed.

2. Materials and methods

2.1. Typical backscattering Mueller matrix images of ex-vivo colon samples

To keep this paper self-contained, we show a typical example of a Mueller image of a colon sample (see Fig. 1), taken from [14]. This image is essentially *diagonal*, which means that the sample behaves as a *pure depolarizer*, without any significant diattenuation or retardation. This sample comprises both healthy (bottom left) and tumoral (top right) regions. At this stage (exophytic growth in the mucosa, with the underlying tissues still untouched) the tumor is less depolarizing than the healthy part. The contrast between the two regions is clearly enhanced in the polarimetric images M_{22}^* and M_{33}^* with respect to the intensity image M_{11} (at the top left corner), showing the potential of the technique for early tumor detection. At subsequent stages, the behavior of the polarimetric response is more complex, as shown in [19,20]. Figure 1 shows a very general trend, observed in virtually all biological tissues: the diagonal matrix elements M_{22}^* and M_{33}^* are almost identical and larger than M_{44}^* .

This means that the sample depolarizing power for an incident linearly polarized light is independent of the polarization azimuth and is smaller than that observed for circular incident polarization. This behavior is typical of Rayleigh or Rayleigh-Gans scattering regimes [14].

Similar images taken at various wavelengths between 500 and 700 nm show an increase of the depolarization power with increasing wavelength. This very general trend is attributed to the decrease of the absorption by the hemoglobin contained in tissue. The absorption

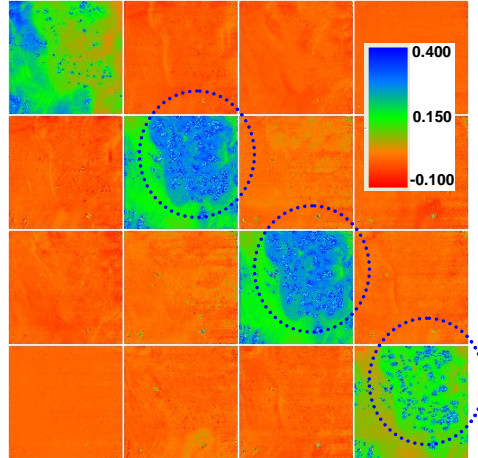


Fig. 1. Mueller matrix image of a colon sample, with a healthy part at the bottom left and a cancerous part at the top right. The matrix is shown in normalized form, with all its elements (except M_{11}) divided by M_{11} and denoted as M^{*}_{ii} ($M^{*}_{ii} = M_{ii}/M_{11}$, $i = 2, 3, 4$) onward. The scale of the normalized elements is given by the colorbar. The image was taken at 550 nm [14,19].

reduces the intensity of the light as it propagates, so with higher absorption, the penetration depth is smaller and, consequently, the average number of scattering events responsible for depolarization also decreases. In this work we present the current state of advancement of our work aimed at defining a realistic, yet tractable model of the polarimetric response of healthy and pathological colon samples.

2.2. Modeling the backscattering from ex vivo colon tissue with Monte Carlo method

2.2.1. Ex-vivo colon tissue structure

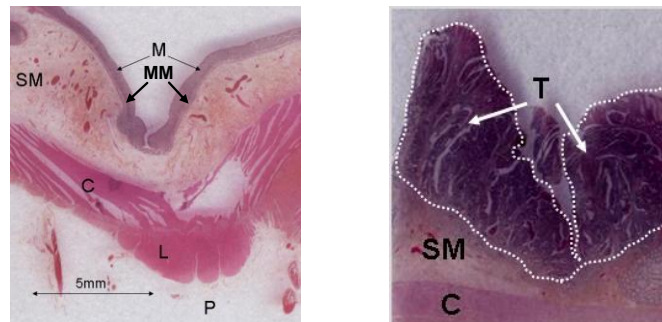


Fig. 2. *Left*: Microscopic structure of a healthy colon sample, with its different layers: the mucosa (M), the submucosa (SM), the circular muscular tissue (C), the longitudinal muscular tissue (L) and the pericolonic tissue (P). The very thin muscularis mucosa (MM) separates M from SM. *Right*: microscopic structure of a pathological sample, with a budding tumor (T) invading the mucosa and submucosa, with the underlying tissues still intact. From Ref. [19].

Normal colon tissue is organized in four layers. From the internal cavity, or lumen, outwards these layers are: the internal coating or mucosa, the middle coat or muscularis externa propria and the external coat or pericolonic tissue (serosa). The mucosa includes a superficial thin layer of epithelium on loose connective tissue. The epithelium is a one-cylindrical-cell layer without capillaries. It receives oxygen and nutriment from the underlying connective tissue by means of exchanges through the basal membrane (BM) that separates the epithelium from the underlying connective tissue which includes capillaries [28]. The BM is a thin layer of specialized extracellular matrix (ECM) that holds the epithelium and where the healthy

epithelial cells regenerate and malignant cells, if present, start proliferating. The ECM is a complex mixture of proteins and carbohydrates which aggregate to form protein molecules with short residual or without carbohydrate chains (such as collagens and elastin) and protein-polysaccharide molecules such as proteoglycan, with much larger amounts of carbohydrates than proteins. The ECM is the main component of the loose connective tissue whose cells are embedded in an amorphous mixture of proteoglycan molecules. In particular, the loose connective tissue of the colon mucosa and submucosa layers is a mesh-like tissue with fluid matrix, whose principal constitutive protein is collagen.

The mucosa is composed of a network of densely arranged very fine collagen fibrils; in contrast the submucosa is almost entirely composed of a dense network of larger collagen fibers. In healthy mucosa the average collagen fibril size is similar to that of the organelles and is of the order of a fraction of a micron. The average size of collagen fibers of submucosa is typically about few microns [26].

The colon mucosa and submucosa layers fold themselves into finger-like shapes for the colon inner part, while for other organs (e.g. uterus) these layers remain flat. As a consequence, when the colon inner surface is observed at a certain distance, the sample may appear as “mixture” of epithelial and connective tissues with the BM close to the surface. The muscularis mucosa (MM) is a very thin layer separating the mucosa from the submucosa and similarly to the submucosa it is composed of a network of densely packed large collagen fibers which scatter light predominantly in the forward direction [26]. Most of the light propagating into the mucosa penetrates into the submucosa. The submucosa comprises larger blood vessels compared to mucosa. As a result, the light incident on the mucosa is more heavily absorbed in the submucosa, especially in the green part of the spectrum, where the hemoglobin features the highest absorption. Hence, only a small fraction of the incident light can penetrate into the deeper layers [24,26,29].

Typically the thicknesses of the mucosa and submucosa are comparable. Moreover, as the muscularis mucosa is very thin and probably features a scattering behavior quite similar to that of the submucosa, in the model it will be lumped together with the submucosa into a single layer, referred to as the submucosa throughout the rest of this paper.

2.2.2. The proposed model of colon optical response

To model the propagation of polarized light in *ex-vivo* colon samples we have represented such samples as multi-layered scattering structures. In a first step we assumed that the mucosa and the submucosa layers consist of a surrounding medium with mono-dispersed scattering spheres. Due to very small thickness of the muscularis mucosa and the similarity between the muscularis mucosa and submucosa optical properties, the muscularis mucosa will be included in the submucosa layer in our model. All underlying layers were lumped into a totally depolarizing Lambertian substrate. In a second step, we considered the layers with bimodal populations representing both the collagen spheres and the sub-cellular organelles - the most important scatterers - within each layer.

We used the description of normal colon tissue proposed in [26] to specify the characteristics of each scattering layer. The scattering spheres with radius r , and optical index n_s were embedded in an extra cellular matrix with optical index n_m . The photon mean free path MFP was defined as $1/N\sigma$, where N is the number density of scatterers and σ is the scattering cross-section [30]. The number density N was calculated from the volume fraction F of the scatterers (i.e. the volume occupied by scatterers per cubic centimeter of sample) as $N = F/V_r$,

where $V_r = \frac{4}{3}\pi r^3$ is the volume of a single spherical scatterer of radius r .

All layers of the virtual sample were placed within a cylinder (diameter 1 cm, variable depth h , see Fig. 3a). The lateral walls of cylinder were assumed to be totally absorbing. The bottom of cylinder was either absorbing or Lambertian substrate. The diffuse illumination ($\lambda = 633$ nm) was propagated along the axis of the cylinder.

Each single layer is thus characterized by the radius r of the scattering spheres, their number density N , which determines the photon mean free path MFP , the optical index contrast, $m = n_s/n_m$; and the layer thickness h_i . For the layer with bimodal population, the radii, number density and optical index contrast of the two types of scatterers are different; r_1 , r_2 , MFP_1 , MFP_2 , m_1 and m_2 .

The semi-infinite Lambertian substrate is a totally depolarizing, partially reflecting medium, such that the intensity of the backscattered light follows the cosine law of the polar angle θ of the scattered light, while being uniformly distributed over the azimuthal angle ϕ . More precisely the intensity $I(\theta, \phi)$ (W sr^{-1}) backscattered into a solid angle $d\Omega$ around the angles (θ, ϕ) is given by:

$$I(\theta, \phi) d\Omega = \frac{aZ_0}{\pi} \cos \theta d\Omega \quad (1)$$

where Z_0 is the illumination power (W) incident on the Lambertian and a its albedo. This is a first approximation of the response of the underlying layers, based on the assumption of a complete randomization of the polarization and emerging direction of the backscattered photons due to a large number of scattering events.

Finally, as shown in Fig. 2, in dysplastic or cancerous colon tissue this structure gets disorganized and its morphology may change with respect to that of healthy tissue. In particular, in cancerous regions the surface may remain flat or may develop an exophytic growth (adenomatous polyps). The possible changes in sample morphology have also been considered in our model by deforming the multilayer structure in two different ways, as shown below.

The stochastic paths of the incident photons were simulated numerically by means of Monte Carlo algorithm. The diffuse light illumination of the sample was modeled with the photons impinging the sample surface at a random location. At each scattering event the changes of photon polarization and direction of propagation were calculated making use of the exact Mie solution for the scattering of plane wave on spherical particle. The implementation of the rejection method and flux-at-point estimation technique allowed us to accelerate the convergence of the statistical algorithm [27].

We first performed the simulation with the single layer model varying the values of model parameters in order to identify the impact of each individual parameter on the ratio of linear to circular polarization of the backscattering light. Then we performed the simulation with the double layer model to find out if the single layer model can be considered as an approximation of the complex multi-layered structure of the colon tissue.

3. Results and discussion

3.1. Multilayered structures with monodisperse scatterers within each layer

3.1.1. Single layer (mucosa) on top of a Lambertian

For the principal model parameters we retained the average values given in [26]. The mucosa tissue was described as a suspension of medium collagen spheres ($r = 200$ nm) at 12% volume fraction in physiological liquid ($MFP = 53.7$ μm , $m = 1.46/1.38$, $h_1 = 0.5$ mm). The submucosa tissue was modeled as a suspension of large collagen spheres ($r = 1.75$ μm), at 50% volume fraction in physiological liquid ($MFP = 19.69$ μm , $m = 1.38/1.36$, $h_2 = 0.7$ mm). No absorption (either from the medium or from the spheres) was taken into account so far.

The value of the Lambertian albedo a was chosen in order to account for the absorption by the mucosa and submucosa layers and the global contribution from the deeper layers. We considered reasonable to vary albedo a values between 0 and 0.3.

In a first instance, we considered the mucosa alone, on top of a Lambertian representing the submucosa and all underlying layers (see Fig. 3a). With nominal values of parameters for mucosa given above and a totally absorbing Lambertian ($a = 0$) the simulated Mueller matrix of the sample obeys the relation:

$$|M_{22}^*| = |M_{33}^*| < |M_{44}^*| \quad (2)$$

This is typical of Mie scattering regime [14]. The albedo a had to be increased to 0.3 to make all the diagonal matrix elements equal, which is not yet what is observed in experiments, namely a M_{44}^* element being significantly smaller than both M_{22}^* and M_{33}^* . As a result, the single layer model with the nominal values of the parameters for the mucosa is certainly not adequate.

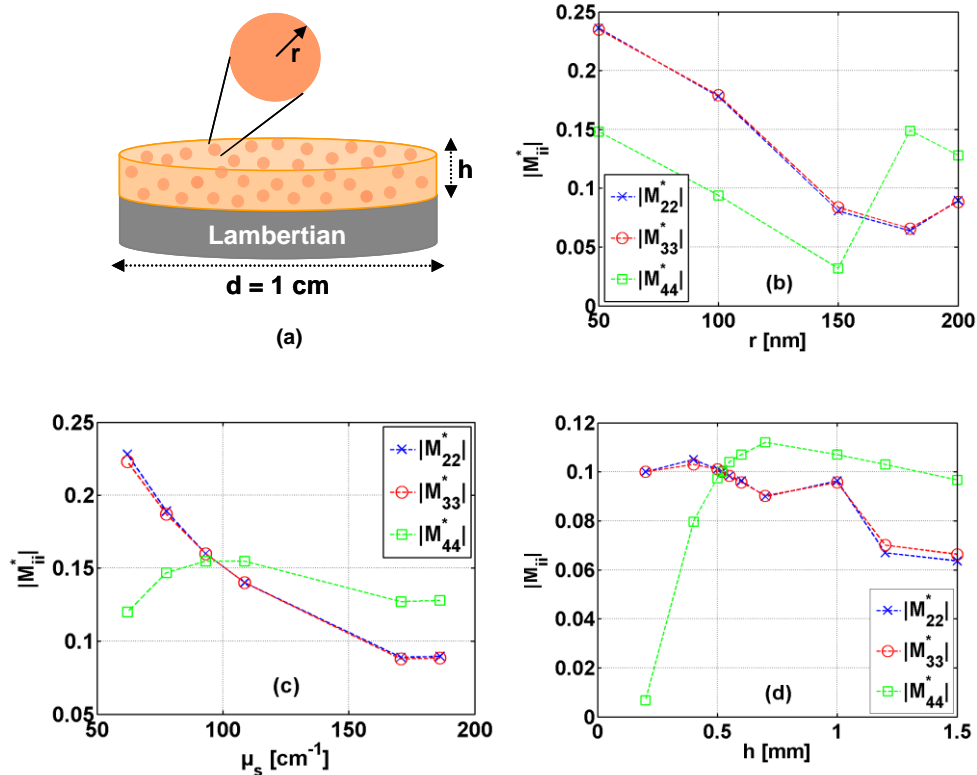


Fig. 3. Absolute values of the diagonal elements $|M_{ii}^*|$ of the backscattering Mueller matrix normalized by $|M_{11}|$, simulated at $\lambda = 633$ nm (a) for mono-dispersed scattering medium on a Lambertian substrate, modeling the mucosa on underlying layers. Each parameter was varied while keeping the others constant at the nominal values for the mucosa ($r = 200$ nm, $MFP = 53.7$ μm ; $m = 1.46/1.38$, $h = 0.5$ mm). (b): variation of the sphere radius r with Lambertian albedo $a = 0$; (c): variation of the scattering parameter with $a = 0$, (d): variation of the scattering layer thickness with $a = 0.3$.

Seeking for the characteristics of the phantom tissue that could reverse the regime of scattering from Mie to Rayleigh-like we tuned the model parameters one by one while keeping others constant. The results are summarized in Fig. 3.

We first decreased the radius of the scattering spheres from 200 nm to 50 nm to determine the typical size of organelles which may reverse the scattering regime from Mie to Rayleigh. It turned out that this regime reversal occurred already at 150 nm radius (Fig. 3b).

Alternatively, we reduced the volume fraction of the 200 nm radius scattering spheres from 12% to 4%, leading to an increase of the light MFP from 53.7 μm to 161.11 μm (or a reduction of $\mu_s = 1/MFP$ from 186.20 to 62.07 cm^{-1}). Increasing the MFP is equivalent to shortening the thickness of the scattering medium, thus reducing the number of scattering events. A transition from Mie to Rayleigh scattering regimes is observed when μ_s decreases, with a threshold at $\mu_s = 0.95$ cm^{-1} (see Fig. 3c). This result suggests that multiple scattering may induce a Mie regime when the number of scattering events is large enough, even for

“small” scatterers, for which a Rayleigh regime would be expected and is indeed observed at lower concentrations.

We also explored the influence of the sample thickness h , between 0.2 and 1.5 mm (Fig. 3d). For this study, the volume fraction of the collagen spheres (with radius 200 nm), was fixed at 6%, corresponding to a MFP of 107.4 μm , so that the experimental criterion was held among the diagonal elements of the Mueller matrix. Moreover, the Lambertian albedo a was set equal to 0.3 to account for the absorption by the medium of the mucosa tissue phantom and the global contribution (absorption and scattering) to the reflected intensity from the layers beneath the mucosa. Figure 3d shows a transition from Rayleigh to Mie regimes when h increases, a result consistent with the previously discussed evolution of the scattering regime with μ_s . When layer thickness h increases, the average number of scattering events increases too, leading to the same trend as that observed when scattering coefficient μ_s increases.

The fact that the simulated Mueller matrices of the sample, described as a suspension of collagen spheres ($r = 200$ nm) at 12% volume fraction in physiological liquid ($MFP = 53.7$ μm , $m = 1.46/1.38$, $h_l = 0.5$ mm) obtained by varying one model parameter (r , MFP , h_l) at time, for reasonable values of the parameters obey to the relation in Eq. (2) typical of Mie scattering, while the occurrence of Mie scattering is never seen experimentally, lead the conclusion that the proposed model of colon tissue is not realistic. It is therefore natural to explore the polarimetric response of more complex structures, which might provide better models of the complex colon tissue structure.

3.1.2. Double layer structure (submucosa and mucosa) on top of the Lambertian

We performed simulations with two superimposed layers, representing the mucosa and submucosa, instead of a single one, on top of the Lambertian substrate. We set the parameters of the mucosa and submucosa layers at the nominal values defined at the beginning of this section. The results of these simulations are shown in Fig. 4.

Histogram (1) represents the diagonal matrix elements of a single layer system representing the submucosa alone, which behaves as a Rayleigh scatterer, but with unrealistically low values of the M_{ii}^* . In contrast, the histograms (2) and (3) of the diagonal Mueller matrix elements, calculated with Lambertian albedos equal to 0.1 and 0.3 respectively, are typical of the Mie scattering regime. Moreover, the absolute values of the $|M_{ii}^*|$ are practically identical to those shown on Fig. 3 for the same parameters of the mucosa scatterers.

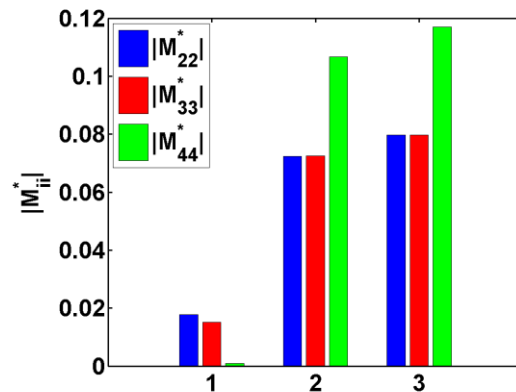


Fig. 4. Absolute values of the diagonal elements of the backscattering Mueller matrix normalized by $|M_{11}|$ simulated at $\lambda = 633$ nm. (1): single layer representing the submucosa ($r = 1.75$ μm , $MFP = 19.69$ μm , $m = 1.38/1.36$, $h = 0.7$ mm) on absorbing substrate (albedo $a = 0$). (2): two layers representing the submucosa (same parameters as above) and mucosa ($r_l = 200$ nm, $MFP = 53.7$ μm , $m = 1.46/1.38$, $h = 0.5$ mm) on Lambertian substrate of albedo $a = 0.1$. (3): same as (2), with $a = 0.3$.

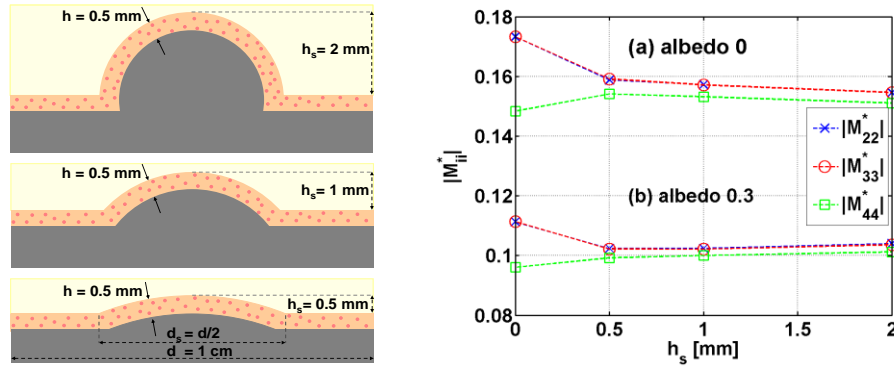


Fig. 5. *Left*: sequence illustrating evolving exophytic growth in colon tissue as uniform (constant thickness) morphological deformation of the superficial layer (mucosa). *Right*: absolute values of the normalized diagonal elements $|M_{ii}^*|$ calculated at $\lambda = 633$ nm for the following scatterer parameters $r = 200$ nm, $\mu_s = 93.1$ cm⁻¹; $m = 1.46/1.38$, $h = 0.5$ mm, albedo $a = 0$ (a) and 0.3 (b).

The fact that the relation between the diagonal elements of the simulated backscattering Mueller matrix image of the multi-layered model remains unchanged compared to that of the single-mucosa-layered model confirms that the single-layered model is a quite good approximation of colon tissue. This observation supports the idea that only a small fraction of the incident light reaches the submucosa layer and an even smaller fraction is backscattered from the submucosa, without any major effect on the total polarimetric response. As a result, in the following we will consider only models with a single layer above the Lambertian.

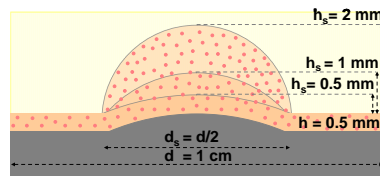
3.1.3. Influence of the layer shapes: simulations of budding tumors

Normally the initial stage of colon cancer development is linked to the growth of a polyp (exophytic growth). So the question arises: can the polarimetric signature of the cancerous part be affected by not only the changes on microscopic level (uncontrolled cell growth, increase in cellular density) but on macroscopic level (morphological transformation of the sample surface) as well? To answer this question we modified the model geometry (see Fig. 5).

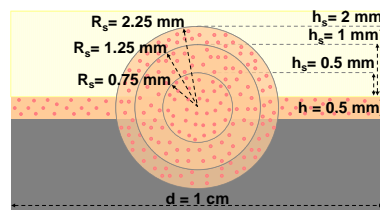
We assumed that the colon tissue undergoes a uniform deformation originating from the deep layers and pushing upwards the flat Rayleigh-like mucosa ($r = 200$ nm, $m = 1.46/1.38$, $MFP = 107.41$ μ m, $h = 0.5$ mm; $a = 0$) while preserving its thickness and optical properties, as in [31]. We also assumed that the exophytic growth covers a surface of a circle with diameter $d_s = 0.5$ cm (which is one half of the diameter d of the whole sample). We performed the simulations for different heights h_s of the bump (0.5 mm, 1 mm, 2 mm) to mimic the incremental growth of the colon tissue deformation. As shown on the right panel of Fig. 5, these morphological changes do not reverse the scattering regime, they only modify the absolute values of the diagonal elements of the Mueller matrix.

However the Rayleigh-like relation between the diagonal elements of the Mueller matrix does not hold anymore when the morphological changes are combined with an increase of the mucosa layer thickness. Figures 6(a, c) represent two different modeled non-uniform deformations of colon tissue originating in the mucosa layer.

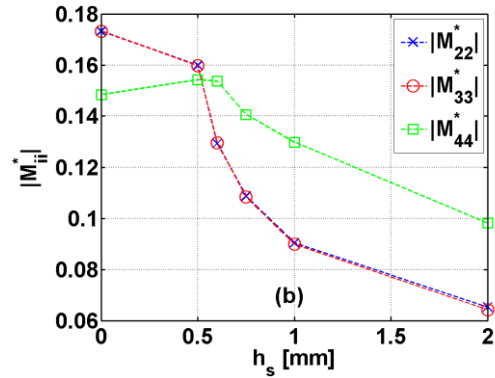
In Fig. 6a the exophytic growth is described as an expansion of the mucosa tissue covering a surface of radius equal to one half of the radius of the initial sample while developing upwards ($R_s = 0.25$ cm; $h_s = 0.5$ mm, 1 mm, 2 mm). In Fig. 6c the exophytic growth is described as a radially symmetric expansion of the mucosa tissue that invades the deeper layer while also developing in height ($R_s = 0.75$ mm, $h_s = 0.5$ mm; $R_s = 1.25$ mm, $h_s = 1$ mm, $R_s = 2.25$ mm $h_s = 2$ mm).



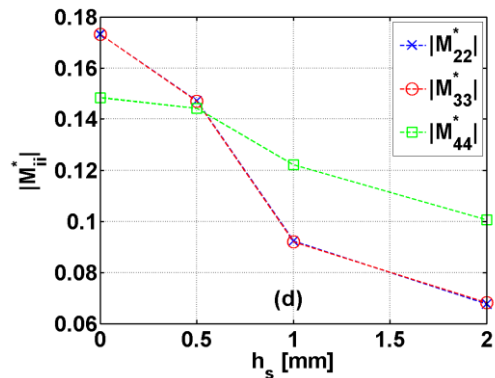
(a)



(c)



(b)



(d)

Fig. 6. *Left*: two illustrations of exophytic growth originating in the mucosa, whose thickness increases in a non-uniform fashion (a, c). *Right*: absolute values of the normalized diagonal elements $|M_{ii}^*|$ of the backscattering Mueller matrix calculated at $\lambda = 633$ nm for a single mucosa layer ($r = 200$ nm, $\mu_s = 93.1$ cm $^{-1}$; $m = 1.46/1.38$, $h = 0.5$ mm) on absorbing substrate (albedo $a = 0$), with h_s varying from 0 (flat surface) to 2 mm (b); or R_s , from 0 to 2.25 mm (d).

The results shown in Figs. 6(b, d) clearly indicate that the scattering regime for the deformed sample changes from Rayleigh-like to Mie when the height/radius of the budding area increases. This trend is consistent with that seen on flat surfaces and shown in Fig. 3d. However we never experimentally observed any inversion for the diagonal coefficients of the measured Mueller matrix images of the light backscattered from healthy or cancerous colon tissue.

The essential conclusion that can be drawn from the results presented in this subsection is thus that the models involving only monodisperse populations of scatterers are prone to switches between the two scattering regimes, for reasonable values of the various parameters, in contradiction with the experimental data. It is therefore mandatory to “stabilize” the model so that in all “realistic” cases the outcome is a Rayleigh scattering regime.

3.2. Multilayered structures with bimodal populations of scatterers

We now consider bimodal populations in each layer, an approach which seems reasonable to better reproduce the variety of scatterers actually found in real tissues. Moreover, due to their isotropic scattering, small scatterers may significantly impact the polarimetric response in the backscattering geometry, even at relatively low concentrations, with a strong Rayleigh type contribution, thus improving the qualitative agreement with experimental data.

In our refined model we represented the scatterers in epithelial cells in the mucosa layer - by their nuclei, the scatterers in connective tissue - by collagen in the extra-cellular matrix, the scatterers in cytoplasm and the extracellular matrix - by sub-organelles in physiological liquid.

In particular we have described the mucosa layer as collagen-like spheres ($r_1 = 200$ nm, $n_2 = 1.46$) and nuclei-like spheres ($R_2 = 3$ μm , $n_2 = 1.4$) or sub-organelles/protein ($r_2 = 50$ nm) in physiological liquid (optical index contrast $m(\lambda) = n_s(\lambda)/n_m$, $n_m = 1.38$; absorption coefficient $\mu_a(\lambda)$) filling the cylinder described above (diameter 1 cm; depth, h), with diffuse illumination at different wavelengths $\lambda = 500, 550, 600, 633, 650, 700$ nm propagating along the axis of the cylinder. We kept the totally depolarizing Lambertian substrate with typical albedo value of 0.3 to model the contribution of the layers beneath the mucosa layer.

The Monte Carlo algorithm was modified in order to take into account the bimodal population of scatterers and a possible absorption by the surrounding medium. The scatterers themselves were still considered as non-absorbing (this limitation will be removed in future work). The overall scattering parameter μ_s of the scattering medium was calculated as the sum of the scattering parameters $\mu_{si} = N_i\sigma_i$ of the embedded monodisperse media. The overall mean free path of the medium is thus

$$MFP = \frac{1}{\sum_i N_i\sigma_i}. \quad (3)$$

The average Mueller matrix of the sample was defined as weighted average of Mueller matrices of the monodisperse media [27].

3.2.1. Preliminary studies with bimodal populations for $\lambda = 633$ nm

To investigate the effect of the sub-organelles we excluded the nuclei from the phantom tissue. The simulations were performed for collagen spheres at 12% volume fraction and varying the volume fraction of the sub-organelles in the phantom tissue from 0.001% to 1% [32], which make the MFP decrease from 55.49 to 53.39 μm ($r_1 = 200$ nm, $r_2 = 50$ nm, $m = 1.058$, $\lambda = 633\text{nm}$) and compared to the simulation without the sub-organelles (monodisperse phantom tissue, $MFP = 53.7$ μm). The insertion of the sub-organelles modified the scattering regime of the phantom tissue already at 0.003% of volume fraction ($MFP = 53.7$ μm , $\mu_s = 186.206$ cm^{-1}) as it is shown in Fig. 7. This trend is certainly due to a rapid increase of the

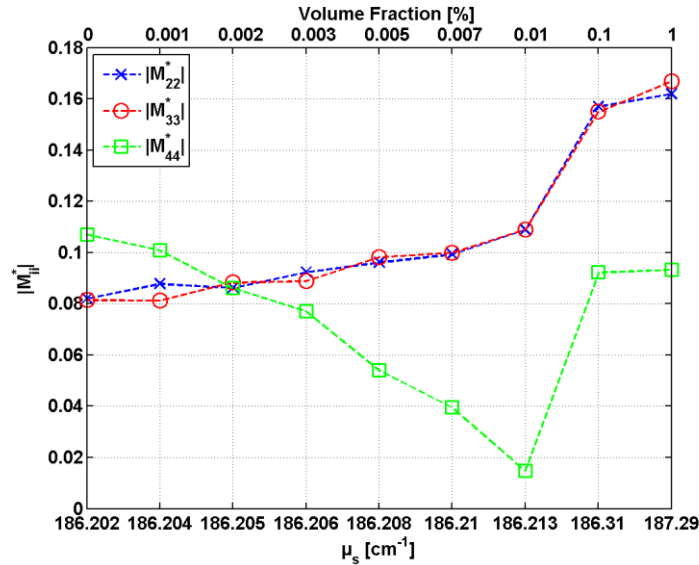


Fig. 7. Normalized diagonal elements of the simulated backscattering Mueller matrices at $\lambda = 633$ nm for a single-layer with a bimodal population of scatterers ($r_1 = 200$ nm; $r_2 = 50$ nm; $m = 1.46/1.38$), Lambertian albedo $a = 0.3$. The images were calculated with r_1 -sphere at 12% volume fraction varying the concentration of r_2 -sphere from 0% (mono-disperse population $\mu_s = 186.202$ cm^{-1}) till 1%.

Rayleigh type contribution due to the small spheres to the backscattered light. Increasing the concentration of the small spheres enhances the Rayleigh type contribution over the Mie type contribution due to the large spheres and strengthens the Rayleigh-like nature of the backscattering from the phantom tissue with bimodal population. It manifests itself as growing divergence between the $|M_{22}^*|$, $|M_{33}^*|$ and $|M_{44}^*|$ values in Fig. 7.

However, to better assess the influence of organelles on the respective magnitudes of $|M_{22}^*|$, $|M_{33}^*|$ and $|M_{44}^*|$ elements, we performed the series of simulations for different layer thicknesses with volume fractions kept constant at 12% for the medium (radius 200 nm) scatterers while the volume fraction for the small (radius 50 nm) scatterers was varied from 0% to 1%. Figure 8 shows the diagonal element values versus layer thickness ranging from 0.5 to 10 mm.

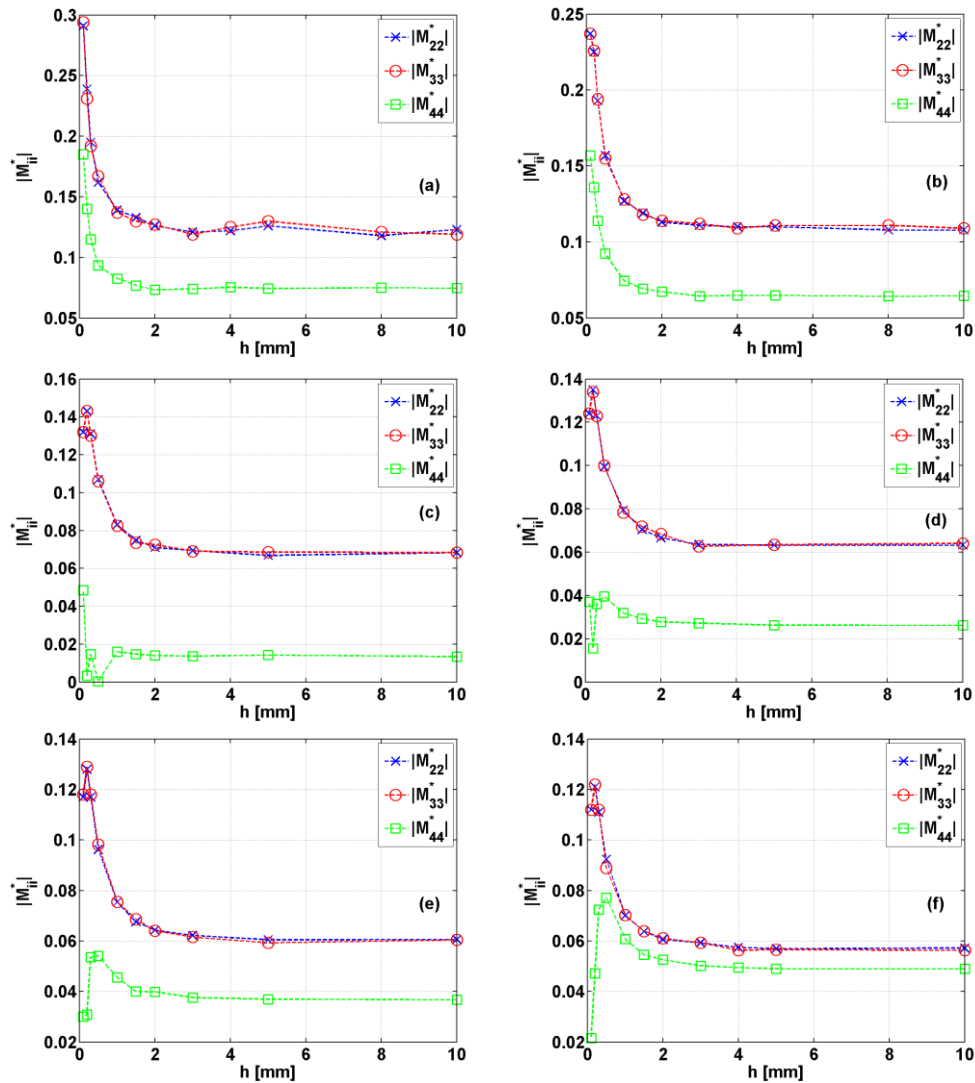


Fig. 8. Normalized diagonal coefficients of the simulated backscattering Muller matrices at $\lambda = 633$ nm for a single-layer with bimodal population of scatterers ($r_1 = 200$ nm; $r_2 = 50$ nm; $m = 1.46/1.38$), Lambertian albedo $a = 0.3$. The images were calculated at different volume fraction of the r_2 -sphere (a): 1%; (b): 0.1%; (c): 0.01%; (d): 0.007%; (e): 0.005%; (f): 0.003%.

We point out that M_{44} coefficient takes negative values as the concentration of the small spheres overpass 0.01% volume fraction, which explains the kink in the curve of $|M_{44}^*|$ in Fig. 7.

In contrast with the monodisperse models investigated in the previous section, the bimodal population model does not change its scattering regime with the layer thickness increase. Moreover, at all concentration of the small scatterers, the diagonal coefficients of the Mueller matrix obey the experimental criterion (Eq. (2)) (Rayleigh scattering regime).

3.2.2. Wavelength dependent polarimetric response

To take into account the wavelength dependence of the simulated results the values of optical index contrast, scattering and absorption coefficients have been calculated as a function of the wavelength from the optical dispersion laws defined in the appendix (Eqs. (6-11)). The results are reported in Table 1. The absorption from the medium was included in the model by modifying the extinction coefficient:

$$\mu_e = \mu_s + \mu_a \quad (4)$$

where μ_s is the scattering coefficient, μ_a is the absorption coefficient. The value of scattering albedo β used in Lambert-Beer law [33–37] was defined as:

$$\beta = \frac{\mu_s}{\mu_s + \mu_a} \quad (5)$$

The data shown in Table 1 suggest that introducing the absorption should hardly change the polarimetric response. The results presented on Fig. 9 clearly confirm this point.

Table 1. Spectrally resolved optical index contrast m , scattering parameter μ_s and absorption coefficient μ_a of the bimodal population tissue phantom

λ [nm]	500	550	600	633	650	700
$m(\lambda) = n_s(\lambda)/n_m$	1.076	1.071	1.066	1.064	1.062	1.059
$\mu_s(\lambda)$ [cm^{-1}]	570.72	394.86	279.29	224.43	201.25	148.27
$\mu_a(\lambda)$ [cm^{-1}]	2.22	4.56	0.70	0.20	0.15	0.09

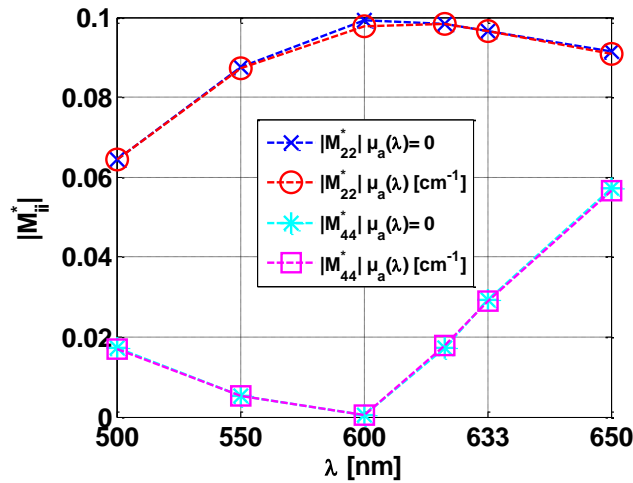


Fig. 9. Spectral dependence of normalized diagonal coefficients of the simulated backscattering Mueller matrices images with diffuse light illumination for single layer bimodal population model of colon tissue ($r_1 = 200$ nm at 12% volume fraction value; $r_2 = 50$ nm at 0.01% volume fraction value, $h = 0.5$ mm, Lambertian albedo $a = 0.3$). The images were calculated using the values of optical index contrast, MFP and absorption coefficient reported in Table 1 in non-absorbing $\mu_a(\lambda) = 0$, and absorbing $\mu_a(\lambda)$ medium.

4. Conclusion

Wavelength dependent ex-vivo measurements of colon tissue show that this tissue behaves as a pure depolarizer throughout the visible spectrum. The relation between the diagonal elements of the experimental backscattering Mueller matrices provides the criterion to discard wrong models of colon tissue. Colon tissue was described using multi-layered model with monodisperse or bimodal populations of scatterers. Monte Carlo simulations of the light backscattered from monodisperse single mucosa layer with 200 nm scatterers showed that the scattering regime switches between Mie and Rayleigh-like regime according to the value of model parameters (scatterer radius r , scattering coefficient μ_s , layer thickness h), implying that the monodisperse single layer (mucosa) model is not adequate for complex colon tissue. Simulated backscattering Mueller matrix images of the double layer (mucosa and submucosa) model with monodisperse (radius 200 nm) mucosa and monodisperse (radius 1.75 μm) submucosa layers illustrated that adding to the model the monodisperse single submucosa layer does not impact the regime of scattering of the monodisperse single mucosa layer. As a result, the single layer (mucosa) model constitutes a valid simplification of colon tissue.

The possible effects of the budding shape of tumors at early stages were also investigated by describing the tumor as a monodisperse scattering layer over a Lambertian, assuming that the budding was due to either the mucosa or the Lambertian. In both cases unrealistic Mie scattering regimes were observed for reasonable parameter values. We therefore concluded that the monodisperse model of the mucosa had to be rejected.

Conversely, the simulations of the backscattering Mueller matrix images of the bimodal population model showed that the mixture comprising small and medium (compared to wavelength) scatterers was in the Rayleigh regime of scattering already at small volume concentration of the small scatterers. Moreover the ratio of linear to circular polarization of the backscattering Mueller matrix of the phantom tissue always obeyed the experimental criterion (see Eq. (2)) while varying the thickness of the layer, a result which was not obtained by simulations involving only monodisperse scatterers with radius 200 nm representing the collagen. This means that the presence of the small scatterers stabilizes the optical response of the phantom tissue in the Rayleigh regime of scattering, ensuring for qualitative agreement between experimental and simulations. The simulations of the backscattering Mueller matrix images of the phantom tissue mixing large (representing the nuclei), medium and small (representing the cell organelles and sub-organelles respectively) scatterers need to be performed to attain quantitative agreement between experiment and modeling. Including the absorption by the medium in our model did not modify the relation between the diagonal elements of the Mueller matrix and their absolute values at all studied wavelengths. However, the absorption cannot be neglected in the realistic model of colon tissue. The next step will be to introduce the absorbing scatterers to the model in order to reproduce the experimentally observed spectral dependence of diagonal elements of the Mueller matrix. The identification of the key model parameters providing quantitative agreement between experimental and modeling at various stages of cancer evolution can help in the interpretation of the experimental data and consequently, in proper cancer staging and early cancer detection.

Appendix A

The dispersion law for collagen was defined as [38,39]:

$$n_{collagen}(\lambda) = 1.426 + \frac{19476}{\lambda^2} - \frac{1131066900}{\lambda^4} \quad (6)$$

where λ is expressed in nm. The medium refractive index was kept constant ($n_m = 1.38$).

The absorption coefficient of the medium was modeled as the sum of the absorption coefficients of hemoglobin, β -carotene [40] and water [41]:

$$\mu_a(\lambda) = \mu_a^{Hb}(\lambda) + \mu_a^{\beta-car}(\lambda) + \mu_a^{water}(\lambda) \quad (7)$$

The absorption coefficient of hemoglobin was corrected by the factor $C_{diff}(\lambda, bvr)$ (<1) suggested by Veen [42] and Svaasand [43] to account for the effects of vessel packing:

$$C_{diff}(\lambda, bvr) = \left\{ \frac{1 - \exp\left[-2 \mu_a^{blood}(\lambda) \right] bvr}{2 \mu_a^{blood}(\lambda) bvr} \right\} \quad (8)$$

Where bvr is the effective blood vessel radius in mm and $\mu_a^{blood}(\lambda)$ is the absorption coefficient of whole blood:

$$\mu_a^{blood}(\lambda) = \ln(10) C_{Hb} \left(\alpha \varepsilon_{HbO_2}(\lambda) + (1 - \alpha) \varepsilon_{Hb}(\lambda) \right) / 64500 \quad (9)$$

where C_{Hb} is the concentration of hemoglobin expressed in mg/mL, α is the degree of oxygen saturation of hemoglobin, $\varepsilon_{HbO_2}(\lambda)$ and $\varepsilon_{Hb}(\lambda)$ are the extinction coefficients of oxygenated and deoxygenated hemoglobin, expressed in $\text{cm}^{-1} \text{mole}^{-1} \text{L}$ [44,45]. C_{Hb} is normally equal to 150 mg/ml. We set the value of 70% for α [26] and the value of 3 μm for bvr , since the diameter of capillary is varied between 5 and 7 μm [29] and its lower limit was estimated as 2.5 μm [40]. The absorption coefficient of the whole blood was multiplied by the volume fraction of blood in tissue V_{Hb} which approximated 2% [26]. The absorption coefficient of hemoglobin is given by the expression:

$$\mu_a^{Hb}(\lambda) = C_{diff}(\lambda, bvr) V_{Hb} \mu_a^{blood}(\lambda) \quad (10)$$

The absorption coefficient of β -carotene (in cm^{-1}) is given by:

$$\mu_a^{\beta-car}(\lambda) = C_{\beta-car} \log(10) \varepsilon_{\beta-car}(\lambda) \quad (11)$$

where the $C_{\beta-car}$ is the concentration of β -carotene [mg/ml] and $\varepsilon_{\beta-car}(\lambda)$ is its extinction coefficient [45].